



A level set method based on additive bias correction for image segmentation

Guirong Weng^{*}, Bin Dong, Yu Lei

School of Mechanical and Electric Engineering, Soochow University, Suzhou 215021, China



ARTICLE INFO

Keywords:

Image segmentation
Intensity inhomogeneity
Additive bias correction
Reflectance image
Level set method

ABSTRACT

Intensity inhomogeneity brings great difficulties to image segmentation. This problem is partly solved by the multiplicative bias field correction model. However, some other problems still exist, such as slow segmentation speed and narrow application field. In this paper, an additive bias correction (ABC) model based on intensity inhomogeneity is proposed. The model divides the observed image into three parts: additive bias function, reflection edge structure function and Gaussian noise. Firstly, the local area and local clustering criterion of intensity inhomogeneity are defined. Secondly, by introducing the level set function, the local clustering criterion is transformed into an energy function based on the level set model. Finally, the structure of the estimated bias field and the reflection edge is computed through the process of minimizing the energy function while the image is segmented. In order to improve the stability of the system, a de-parameterized regularization function and an adaptive data-driven term function are designed. Compared with the traditional multiplicative model, the addition model has faster calculation speed. The proposed model can obtain ideal segmentation effect for images with intensity inhomogeneity. Experiment results show that the proposed method is more robust, faster and more accurate than traditional piecewise and multiplicative models.

1. Introduction

Image segmentation technology is a significant research content in the fields of computer vision, artificial intelligence and image processing (Banan, Nasiri, & Taheri-Garavand, 2020; Fan, Xu, Wu, Zheng, & Tao, 2020; Huang & Chau, 2008; Jia, Ling, Chau, & Heutte, 2008; Cai, Liu, Zhou, Sun, & Li, 2018; Golam Moazzam, 2013; Chan et al., 2018). Active contour models based on level set method have become the hot spot of image segmentation. Active contour models are roughly divided into edge-based models (Caselles, Catté, Coll, & Dibos, 1993; Vicent, Ron, & Guillermo, 1997; Li, Xu, Gui, & Fox, 2010; Jin & Weng, 2019d; Jin & Weng, 2019c), region-based models (Chan & Vese, 1977; Li, Kao, Gore, & Ding, 2007; Li, Kao, Gore, & Ding, 2008; Ding, Xiao, & Weng, 2017; Jin & Weng, 2019a) and multiplicative bias correction model (Li et al., 2011; Li, Gore, & Davatzikos, 2014; Zhang, Zhang, Lam, & Zhang, 2016; Zhou, Wang, Zhang, Cai, & Gong, 2017; Jin & Weng, 2019b; Dong, Jin, & Weng, 2019). Edge-based models use edge indicators to guide the curve toward the target boundary, such as the geodesic active contours (GAC) model (Vicent et al., 1997). For the image with weak edge and

noise, the segmentation effect of edge-based models is not good. Based on the region-based models, specific image descriptors are used to partition the image domain. These kinds of models can effectively segment images with weak boundaries, while they are more sensitive to strong noise or uneven grayscale. The Chan-Vese (CV) model (Chan & Vese, 1977) and the region-scalable fitting (RSF) model (Li et al., 2008) are two classic region-based active contour models. Based on the CV model, the RSF model uses local image information to solve the problem of intensity inhomogeneity. However, the segmentation speed of the RSF model is poor and the initial contour is sensitive. Li et al proposed a bias correction (BC) model (Li et al., 2011) to further enrich theory in the CV model and provide an effective algorithm for level set function in image segmentation. It also provides new directions for future image segmentation. Meanwhile, the BC model has the following problems:

1. The BC model uses multiple Gaussian convolutions, which greatly increases the running time.
2. The BC model is sensitive to inconsistent lighting images.

* Correspondence author: School of Mechanical and Electric Engineering, Soochow University, No. 178, Ganjiang Road, Suzhou City, Jiangsu Province 215021, China.

E-mail addresses: wgr@suda.edu.cn (G. Weng), 20184229019@stu.suda.edu.cn (B. Dong), 20195229078@stu.suda.edu.cn (Y. Lei).

Table 1

The CPU runtime, the IOU and the IOU1 of the images in Fig. 6. (Runtime(s)/IOU/IOU1).

	RSF	LIF	ABC
I1 (228*300)	9.70/0.54/0.98	2.24/0.53/0.98	3.94/0.58/0.98
I2 (300*270)	17.9/0.81/0.95	35.1/0.83/0.96	6.14/0.83/0.96
I3 (300*225)	12.4/0.84/0.94	14.5/0.85/0.95	5.17/0.93/0.98
I4 (120*90)	6.94/0.52/0.94	0.39/0.78/0.98	0.28/0.83/0.99
I5 (481*321)	33.4/0.87/0.99	17.3/0.84/0.98	3.62/0.88/0.99
I6 (481*321)	45.3/0.63/0.97	40.2/0.80/0.99	8.19/0.85/0.99

3. The BC model has a poor effect on the image segmentation with local intensity inhomogeneity. The derived bias estimation changes too slowly to reflect some false targets in the image.

This paper aims to improve the shortcomings of the above active contour models and proposes an image synthesis model based on the addition feature, which improves the segmentation efficiency and enhances the robustness. The addition model converts the multiplication operation of image matrix into addition operation, which improves the calculation speed. Our model also designs a de-parameterized regularization function and an adaptive data-driven term function. There is no coefficient that needs to be adjusted repeatedly in Eq. (26), which improves the robustness of the model. The proposed model based on addition image model can be better applied to various image segmentation, especially in the field of medical images Table 1.

2. Background

Let $\Omega \in \Re^2$ be the image range. $I : \Omega \rightarrow \Re$ is the given grayscale image. C is a contour within the image area Ω , which divides the image domain into two parts: $\Omega_1 : \text{outside}(C)$ and $\Omega_2 : \text{inside}(C)$.

In 1974, Horn et al. proposed the multiplicative model of images (Horn, 1974), which analyzed and solved the illumination problem. In order to solve the problem of intensity inhomogeneity in image segmentation, the real image can be described as a method of synthesizing image model. The multiplication model is redefined and the observed image can be modeled as:

$$I(x) = b(x)J(x) + n(x) \quad (1)$$

Where J is the real image, which represents the intrinsic physical characteristics of the image. b is the component with uneven intensity and n is the additional noise. b is also called the bias field. The assumptions about the real image and the bias field are specified as follows:

- (1) The bias field b is slowly changing. Therefore, we can assume that the bias field b is approximately constant in the neighborhood of each point in the image domain.
- (2) J can be assumed to be a approximate piecewise constant (Ding et al., 2017). Real images J in the region of the disjoint $\Omega_1, \dots, \Omega_N$ are taken in N different constant c_1, \dots, c_N . Where $\{\Omega_i\}_{i=1}^N$ respectively form the image domain partition according to the model in Eq. (1), which is expressed as $\Omega = \cup_{i=1}^N \Omega_i$ and $\Omega_i \cap \Omega_j = 0 (i \neq j)$.

The theory of bias field image model and bias correction assumptions has been widely accepted and applied. At present, most of the bias field active contour models adopt the following multiplicative model and bias correction assumptions.

Li et al proposed the bias correction (BC) model (Li et al., 2011). The following energy function is derived by using the local clustering criterion function:

$$\varepsilon = \int \left(\sum_{i=1}^N \int_{\Omega_i} K(y-x) |I(x) - b(y)c_i|^2 dx \right) dy \quad (2)$$

Where c_1, \dots, c_N is the constants. The kernel function $K(u)$ is selected as a truncated Gaussian function and is defined as follows:

$$K(u) = \begin{cases} \frac{1}{\alpha} e^{-|u|^2/2\sigma^2}, & \text{for } |u| \leq p \\ 0, & \text{otherwise} \end{cases} \quad (3)$$

Where α is a normalized constant. Function $K(u)$ has the following equation relation: $\int K(u) = 1$. σ is the standard Gaussian deviation. p is the radius of the neighborhood Ω_y .

By exchanging the order of the integrals and considering the energy in two-phase level set function, Eq. (2) can be expressed as the following level set function:

$$\varepsilon(\varphi, c, b) = \int \left(\sum_{i=1}^2 \int K(y-x) |I(x) - b(y)c_i|^2 dy \right) M_i(\varphi) dx \quad (4)$$

Where $M_1(\varphi)$ and $M_2(\varphi)$ are defined as $M_1(\varphi) = H(\varphi)$ and $M_2(\varphi) = 1 - H(\varphi)$, respectively. $H(\varphi)$ represents the Heaviside function. The vector c represents the constant c_1, \dots, c_N . The level set function φ , vector c and bias field b are variables of energy $\varepsilon(\varphi, c, b)$. Bias field b and piecewise constant c are as follows:

$$\hat{c}_i = \frac{\int (b^* K) I u_i dy}{\int (b^* K) u_i dy}, \quad i = 1, 2 \quad (5)$$

$$\hat{b} = \frac{(IJ^{(1)})^* K}{J^{(2)*} K} \quad (6)$$

Where $u_i = M_i(\varphi(y))$, $J^{(1)}$ and $J^{(2)}$ are expressed as $J^{(1)} = \sum_{i=1}^N c_i u_i$ and $J^{(2)} = \sum_{i=1}^N c_i^2 u_i$, respectively. The kernel function $K(u)$ ensures the slowly varying nature of the derived optimal bias field estimation.

The above defined energy $\varepsilon(\varphi, c, b)$ is used as the data term in the energy of the proposed variational level set formulation, which is defined by

$$F^{BC}(\varphi, c, b) = \varepsilon(\varphi, c, b) + \nu L(\varphi) + \mu R(\varphi) \quad (7)$$

Minimizing the energy functional F^{BC} with respect to φ by the standard gradient descent method, we obtain the variational level set formulation as follows:

$$\frac{\partial \varphi}{\partial t} = -\delta(\varphi)(e_1 - e_2) + \nu \delta(\varphi) \operatorname{div} \left(\frac{\nabla \varphi}{|\nabla \varphi|} \right) + \mu \operatorname{div} (d_p(|\nabla \varphi|) \nabla \varphi) \quad (8)$$

Where Heaviside function is defined as $H(\varphi) = \frac{1}{2} \left(1 + \frac{2}{\pi} \arctan \left(\frac{\varphi}{\epsilon} \right) \right)$.

Its derivative is defined as $\delta(\varphi) = \frac{1}{\pi} \left(\frac{\epsilon}{\epsilon^2 + \varphi^2} \right)$.

3. The proposed model

3.1. Image model and problem formulation

In 1974, Horn et al. proposed a retinex mathematical model (Horn, 1974). They considered the problem of the bottom reflection ratio r . According to the reflection ratio r and illumination b , the observed intensity i was expressed:

$$i(x, y) = b(x, y) + r(x, y) \quad (9)$$

Where $i = \log(I)$. With reference to Eq. (9) and bias correction assumptions in Section Background, this paper introduces the bottom reflection ratio into the treatment of uneven intensity, we make the following assumptions:

- (A) In the local region, the intensity inhomogeneity b should be smoothly changed. Therefore, the components of the intensity in-

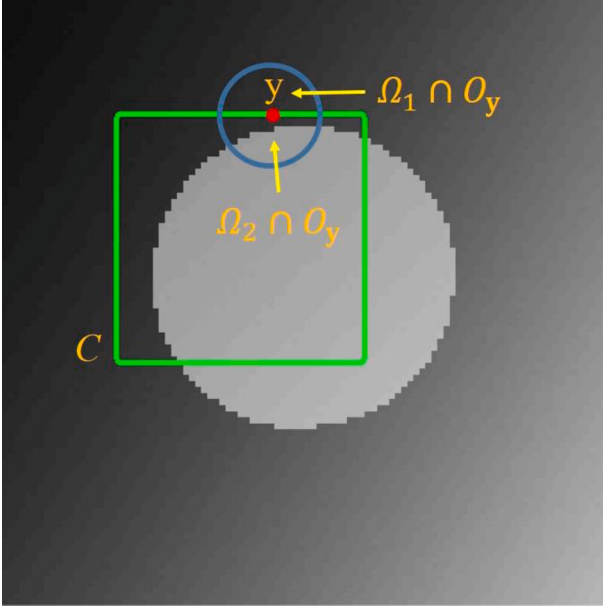


Fig. 1. Description of region O_y , Ω_1 and Ω_2 .

homogeneity in the image disjoint regions $\Omega_1, \dots, \Omega_N$ take N different fitting functions $b_1(x), \dots, b_N(x)$. Where $\{\Omega_i\}_{i=1}^N$ forms the partitions $\Omega = \cup_{i=1}^N \Omega_i$ and $\Omega_i \cap \Omega_j = \emptyset (i \neq j)$ of the image domain according to Eq. (9).

(B) The observed spatial derivative of the intensity is mainly composed of the structure of the edge in the reflection ratio r . Therefore, we can integrate this new retinex model into the level set model. Consider the piecewise invariant parts of the image, the intensity inhomogeneity of the local area with smooth changes can be estimated.

Then the image can be modeled as:

$$i(x) = b(x) + r(x) + n(x) \quad (10)$$

Where b is the component with uneven intensity (bias field image). r represents the structure of the edge in the spatial derivative reflectance of the observed intensity. r is also called the reflected image. n represents the zero mean Gaussian noise. The proposed addition model transforms the multiplication operation of image matrix into addition operation, which reduces the computation time and improves the segmentation speed.

3.2. Criterion functions

According to the above image model and assumptions (A) and (B), Eq. (10) is rewritten and described as follows:

First, define a circular neighborhood (or rectangular neighborhood) with radius ρ , which is centered on each point $y \in \Omega$ defined by $O_y = \{x : |x - y| \leq \rho\}$. The partition $\{\Omega_j\}_{j=1}^N$ of the whole domain Ω induces the partition of the neighborhood O_y , that is, $\{O_y \cap \Omega_j\}_{j=1}^N$ forms the partition of O_y . For a slowly varying bias field b , the intensity of each partition $O_y \cap \Omega_j$ is replaced by $b(x)$, where $x \in O_y \cap \Omega_j$. If we divide the whole domain Ω into two subregions: Ω_1 and Ω_2 , the dividing line of Ω_1 and Ω_2 can be represented by curve C . Due to the characteristics of δ during computing, only the data of the small region near the narrow band of curve C is calculated. To solve this problem, a truncation function $G(y - x)$ is defined to be introduced into subregions Ω_1 and Ω_2 . The truncated Gaussian function $G(y - x)$ is defined as follows:

$$G_\sigma(y - x) = \begin{cases} \frac{1}{\beta} e^{-|y-x|^2/2\sigma^2}, & \text{for } |y - x| \leq \rho \\ 0, & \text{otherwise} \end{cases} \quad (11)$$

Where β is a normalized constant and σ is the standard deviation (or scale parameter) of the Gaussian. The function of truncated Gaussian function is to ensure that the influence of partial field value of point y on local energy decreases to zero when the distance difference between pixel x and pixel y exceeds ρ . The following equation relation can be obtained by integrating the Gaussian kernel: $\int G(u) du = 1$.

Because of the truncation function $G(y - x)$, the value outside O_y is zero. Then O_y can be merged into Ω_1 and Ω_2 , which is shown in Fig. 1. Therefore, $x \in O_y \cap \Omega_j$ can be directly rewritten as $x \in \Omega_j$. The bias field b of each partition can be represented by $b_j(x)$, where $x \in \Omega_j$.

Therefore, the image model in Eq. (10) can be rewritten as:

$$i(x) \approx b_j(x) + r(x) + n(x) \quad \text{for } x \in \Omega_j \quad (12)$$

3.3. Energy functions

The description of the criterion functions above can be used to dichotomize the local intensity with K-means++ clustering algorithm (Li et al., 2011; Li et al., 2007). K-means++ clustering algorithm is an iterative calculation process of neighborhood intensity. The following energy function is defined by the minimum clustering criterion algorithm:

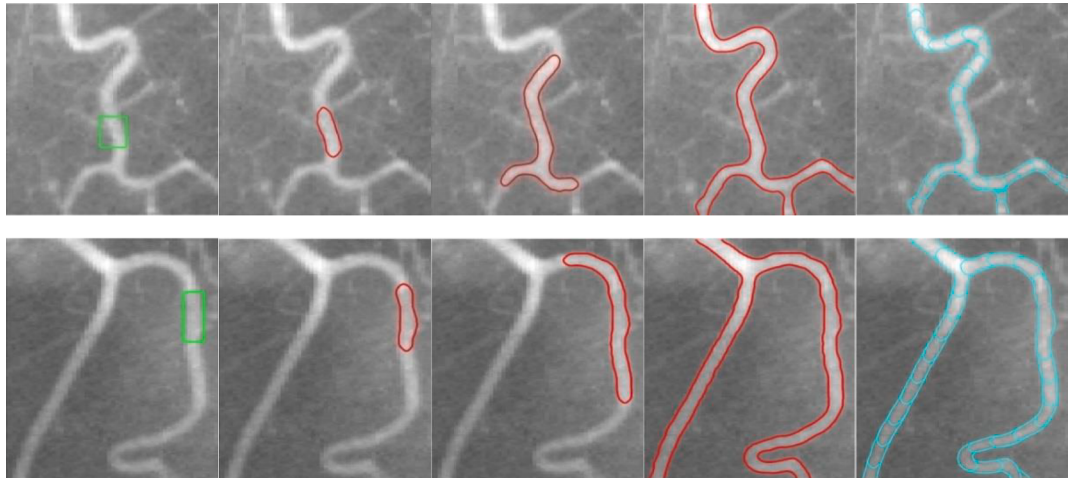


Fig. 2. Segmentation results by the ABC model. From left to right: original image with initial contours, segmentation result of every three iterations, segmentation result of every fifteen iterations, final segmentation results and the iterative process, respectively.

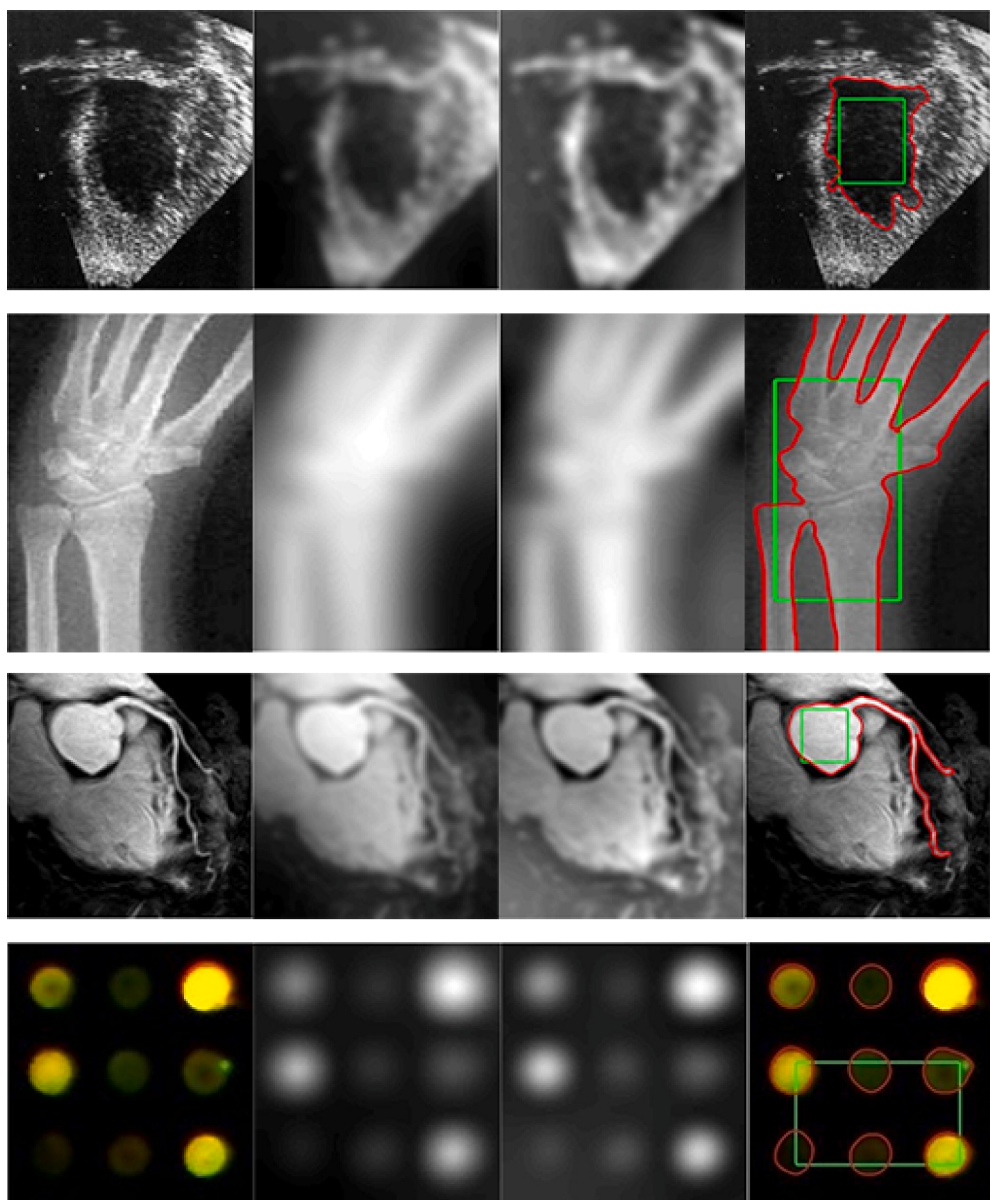


Fig. 3. Segmentation results for four images with different imaging principles. From left to right: original image, additive bias image, reflection image and segmentation results, respectively.

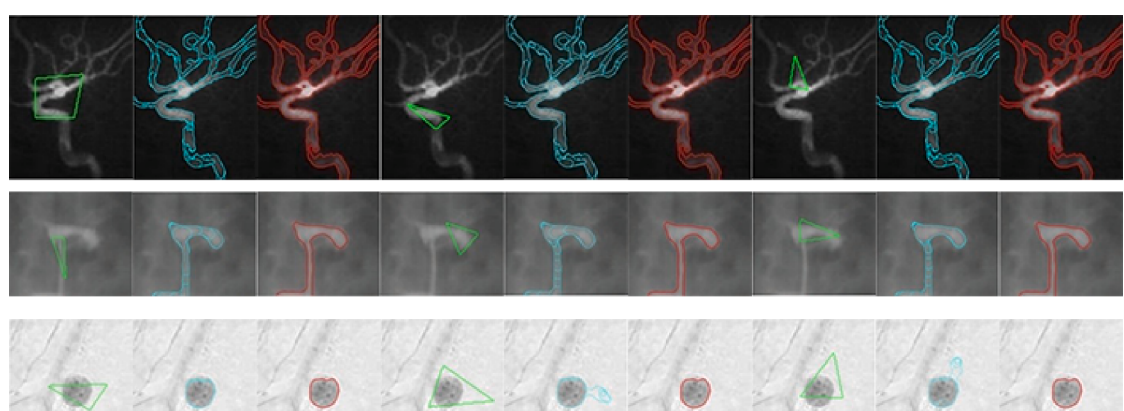


Fig. 4. Segmentation results by the ABC model under different initializations. In each group of images, from left to right: original image with initial contours, iterative process and segmentation results, respectively.

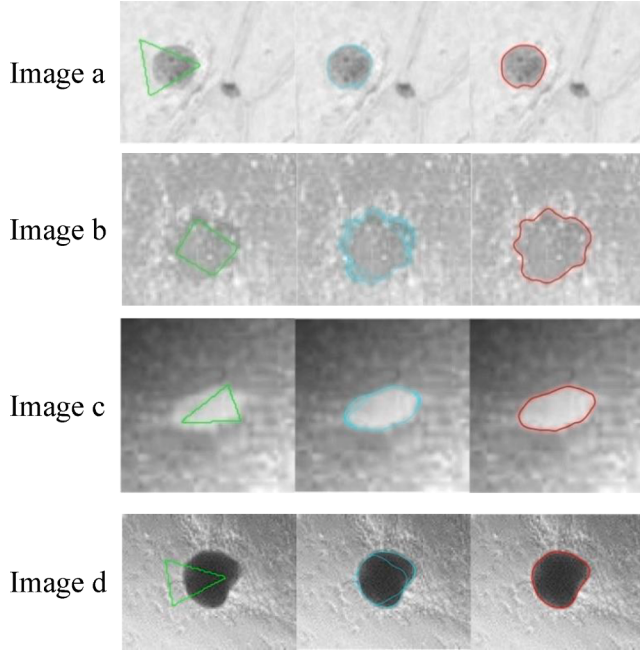


Fig. 5. Segmentation results by the ABC model under strong noise. From left to right: original images and initial contours, the iterative process of segmentation and segmentation results, respectively.

$$F_y = \sum_{j=1}^2 \int_{\Omega_y} |i_r(\mathbf{x}) - c_j|^2 u_j(\mathbf{x}) d\mathbf{x} \quad (13)$$

Where $i_r(\mathbf{x}) = i(\mathbf{x}) - r(\mathbf{x})$. Therefore, the cluster center $c_j \approx b_j$. u_j represents a membership function used to determine whether \mathbf{x} is within the region Ω_j . Its membership is: $u_j(\mathbf{x}) = 1, \mathbf{x} \in \Omega_j$ and $u_j(\mathbf{x}) = 0, \mathbf{x} \notin \Omega_j$. Since u_i is a membership function related to Ω_j , F_y can be rewritten as:

$$F_y = \sum_{j=1}^2 \int_{\Omega_y} |i_r(\mathbf{x}) - b_j(\mathbf{x})|^2 d\mathbf{x} \quad (14)$$

For the clustering criterion in Eq. (14) and the clustering center approximated by $c_j \approx b_j$, we can merge Ω_y into region Ω_j according to the truncated Gaussian function. Therefore, the above criteria are redefined to unify the intensity classification area in Ω_y . The function is as follows:

$$F_y = \sum_{j=1}^2 \int_{\Omega_j} G_\sigma(\mathbf{y} - \mathbf{x}) |i(\mathbf{x}) - r(\mathbf{y}) - b_j(\mathbf{y})|^2 d\mathbf{x} \quad (15)$$

For all \mathbf{y} in the whole image region, we need to minimize F_y . In the proposed method we use the integral of \mathbf{y} to minimize F_y . Its energy function is as follows:

$$F = \int \left(\sum_{j=1}^2 \int_{\Omega_j} G_\sigma(\mathbf{y} - \mathbf{x}) |i(\mathbf{x}) - r(\mathbf{y}) - b_j(\mathbf{y})|^2 d\mathbf{x} \right) d\mathbf{y} \quad (16)$$

In Eq. (16), the integral domain is on the whole region Ω . The reflection image r and bias field b_j in region Ω_j are computed respectively to minimize Eq. (16) and complete the image segmentation.

In the level set method, a Lipschitz function $\varphi : \Omega \rightarrow \mathbb{R}$ is introduced. It belongs to the symbol set function and can be used to represent two disjoint subregions Ω_1 and Ω_2 . Then the regions Ω_1 and Ω_2 are defined by $M_1(\varphi) = H(\varphi)$ and $M_2(\varphi) = 1 - H(\varphi)$. Through setting $\mathbf{b} = (b_1, b_2)$, the energy in Eq. (16) can be rewritten in the following form:

$$E^{ABC}(\varphi, r, \mathbf{b}) = \int \sum_{j=1}^2 \left(\int G_\sigma(\mathbf{y} - \mathbf{x}) |i(\mathbf{x}) - r(\mathbf{y}) - b_j(\mathbf{y})|^2 d\mathbf{y} \right) M_j(\varphi(\mathbf{x})) d\mathbf{x} \quad (17)$$

The calculation of energy minimization is performed below. For fixed φ and r , the optimal \mathbf{b} that minimizes the energy $E^{ABC}(\varphi, r, \mathbf{b})$ is expressed as:

$$\hat{b}_j(\mathbf{x}) = \frac{G_\sigma^*((i - r)M_j(\varphi))}{G_\sigma^*M_j(\varphi)}, j = 1, 2 \quad (18)$$

Next, optimize the algorithm of Eq. (18) and the result is shown in Eq. (19). G_σ^*1 is calculated only once before iteration. During the iteration, only three convolutions are calculated, which is shown as:

$$\begin{cases} \hat{b}_1(\mathbf{x}) = \frac{G_\sigma^*((i - r)H(\varphi))}{G_\sigma^*H(\varphi)} \\ \hat{b}_2(\mathbf{x}) = \frac{G_\sigma^*(i - r) - G_\sigma^*((i - r))^*H(\varphi)}{G_\sigma^*1 - G_\sigma^*H(\varphi)} \end{cases} \quad (19)$$

Where $G_\sigma^*H(\varphi)$, $G_\sigma^*(i - r)$ and $G_\sigma^*((i - r)H(\varphi))$ need to be computed during the iteration.

For fixed φ and \mathbf{b} , the optimal r that minimizes the energy $E^{ABC}(\varphi, r, \mathbf{b})$ is expressed as:

$$\hat{r}(\mathbf{x}) = \frac{G_\sigma^*[(i - b_1)H(\varphi) + (i - b_2)(1 - H(\varphi))]}{G_\sigma^*1} \quad (20)$$

Analyze the local area problem in Eq. (17) and extract its data items as follows:

$$e_j(\mathbf{x}) = \int G_\sigma(\mathbf{y} - \mathbf{x}) |i(\mathbf{x}) - r(\mathbf{y}) - b_j(\mathbf{y})|^2 d\mathbf{y} \quad (21)$$

$$E^{ABC}(\varphi, r, \mathbf{b}) = \int \sum_{j=1}^2 e_j M_j(\varphi(\mathbf{x})) d\mathbf{x} \quad (22)$$

Minimizing the energy functional $E^{ABC}(\varphi)$ with respect to φ using the standard gradient descent method, we obtain the variational level set function as follows:

$$\frac{\partial \varphi}{\partial t} = -\frac{\partial E^{ABC}}{\partial \varphi} = -\delta(\varphi)(e_1 - e_2) \quad (23)$$

Eq. (23) is derived based on the additive bias field model. This function considers the intensity inhomogeneity and local characteristics of the image, which is an optimization of the CV model. In practical applications, due to the variety of image types, the data-driven term $e_1 - e_2$ in Eq. (23) differs greatly, which will increase the difficulty of experiments and reduce the robustness of the system. For this reason we introduce an activation function. The range of the activation function is $(-1, 1)$. This function is an odd function. Its function image is a strictly monotonically increasing curve that passes through the origin and crosses quadrants I and III. Its image is limited to two horizontal asymptotes: $y = 1$ and $y = -1$. The data of the activation function near the zero point is more sensitive. In this way, we smooth the data with large differences and increase the sensitivity of the data with smaller differences in the data-driven terms, which is helpful to accurately locate the boundary. In addition, an adjustable coefficient α is added. We have rewritten Eq. (23) as:

$$\frac{\partial \varphi}{\partial t} = -\alpha \delta(\varphi) \tanh((e_1 - e_2)/\beta) \quad (24)$$

$$\beta = \sqrt{\frac{1}{M \times N} \sum_{i=1}^M \sum_{j=1}^N (I(i, j) - \bar{I}(i, j))^2} \quad (25)$$

An image standard deviation β is added in Eq. (24) to the denominator of the data driver term. The standard deviation β of the image reflects the discrete relationship of the binary image. The smaller the β is, the closer the distance between the target and the background is, while the smaller the difference of the data driver is. The added coefficient α can improve the robustness of Eq. (24). Coefficient α has the ability of adaptive adjustment. For pictures with different sizes and

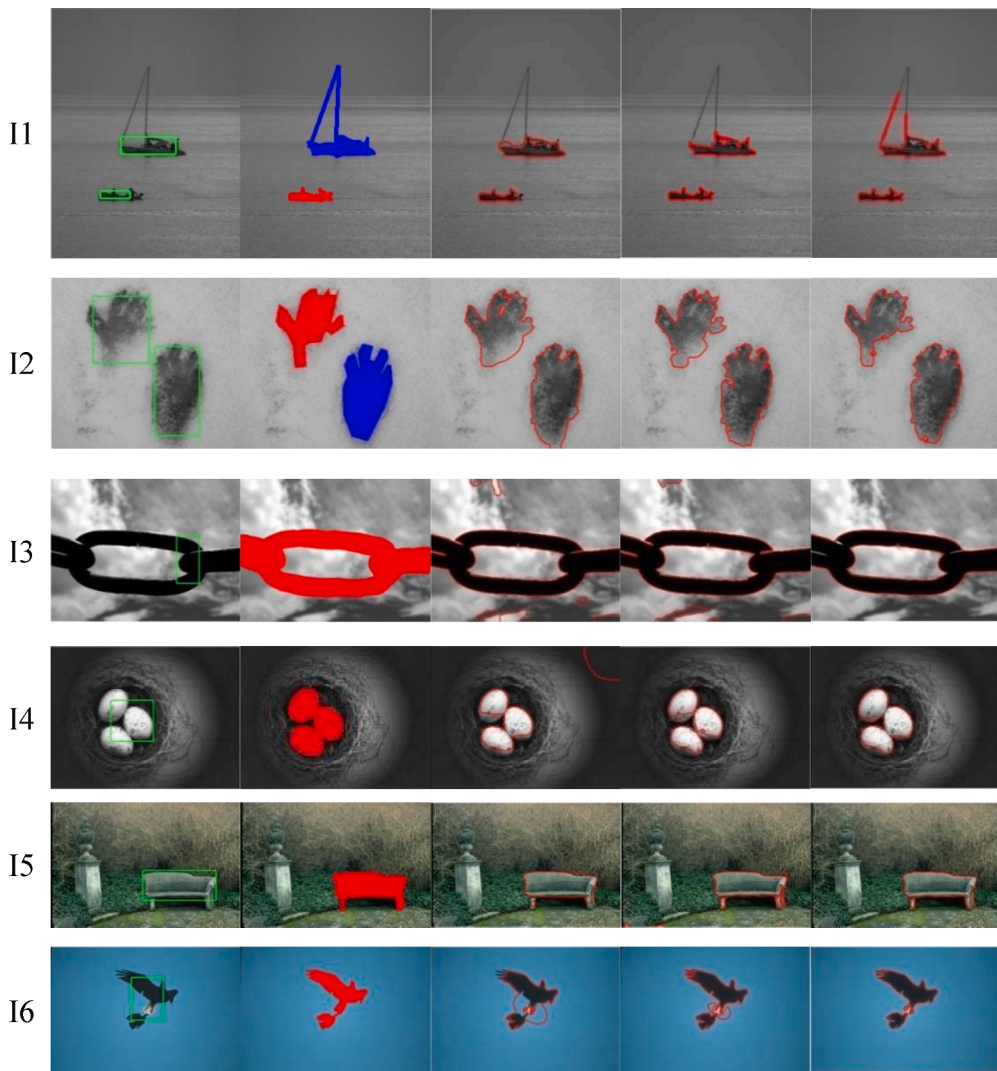


Fig. 6. Comparison experiment with two local region-based ACMs. From left to right: original images with initial contours, segmentation results in the standard image libraries, segmentation results by the RSF, LIF and ABC models, respectively.

features, there is no need to adjust the parameters repeatedly.

3.4. Length term function and regularization method

There is only one energy term in Eq. (24), without the traditional length term $L(\varphi)$ and regularization $R(\varphi)$. In the level set method, regularization is to ensure that the sign distance function of the interface of the level set function is kept during the evolution process. It also prevents the level set function from being too steep or too flat. Li et al. [26] proposed the average formula of penalty level set function deviating from sign distance function. This method reduces the computation to some extent. However, this method is sensitive to initialization (Li et al., 2000). Later, Zhang et al. proposed the local image fitting (LIF) model (Li et al., 2010), which uses Gaussian filtering instead of regularization in the level set function. In this strategy, the standard deviation of the gaussian filter can be used to control the regularization intensity, just like the parameters μ in the RSF model. Smooth regularization is replaced by $\varphi^{n+1} = G_{\sqrt{\Delta t}} * \varphi^n$, where Δt is the time step and $G_{\sqrt{\Delta t}}$ is a Gaussian kernel with scale parameters Δt . The analysis shows that the gaussian smoothing filter of the LIF model makes the contour smooth and prevents the level set function from being too steep, while makes the level set curve too flat, which is not conducive to the determination of the boundary.

According to the above analysis, the regularization function should ensure that the level set function f has enough sensitivity at zero crossing, while remaining smooth in the region away from the zero-level set. In order to effectively carry out robust regularization of the level set function, this paper defines a de-parameterized regularization function:

$$\varphi_R = \tanh(\eta \varphi^{n+1}) \quad (26)$$

Where η is set to a fixed constant 7. The purpose of Eq. (26) is to improve the slope of the level set function in the zero-crossing region and suppress the slope of the two high points. The proposed de-parameterized regularization function adopts the nonlinear stretching method to keep the range of the function unchanged, improve the slope of the function passing the zero point, and smooth the other regions to achieve the regularization of the level set function. In addition, there is no coefficient that needs to be adjusted repeatedly in Eq. (26), which improves the robustness of the model.

In the process of E^{ABC} minimization, the zero-level set curve C will gradually include the boundary line of the edge structure that satisfies the rules. However, there will be some extra curves in other areas or places with strong noise. In addition, the curve of the zero-level set C will become rugged due to the difference in exercise intensity and direction. Therefore, it is necessary to add a function to perform the same function as the length constraint term $L(\varphi)$ for smoothing and shortening

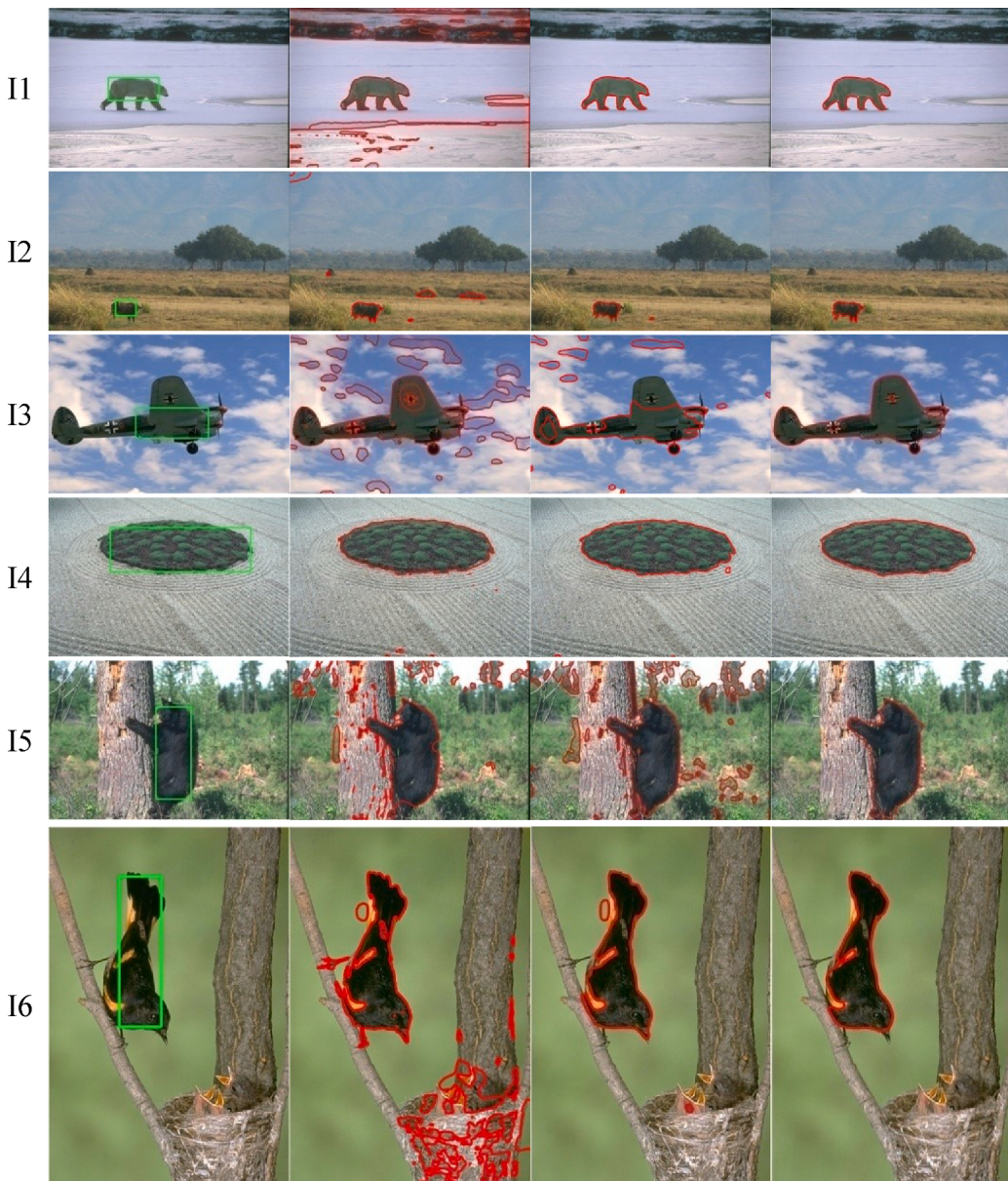


Fig. 7. Comparison experiment with two state-of-the-art ACMs. From left to right: original images and initial contours, segmentation results by the RSF&LoG, LPF&FCM and ABC models, respectively.

Table2

The CPU runtime, the IOU and the IOU1 of the images in Fig. 7. (Runtime(s)/IOU/IOU1).

	RSF&LoG	LPF&FCM	ABC
I1 (481*321)	14.3/0.18/0.84	12.1/0.91/0.99	2.09/0.91/1.00
I2 (481*321)	16.3/0.48/0.99	11.9/0.81/1.00	2.43/0.88/1.00
I3 (481*321)	27.1/0.50/0.85	16.2/0.55/0.91	10.7/0.90/0.98
I4 (481*321)	16.2/0.96/0.99	15.5/0.96/0.99	2.13/0.97/0.99
I5 (481*321)	21.5/0.58/0.91	19.9/0.50/0.87	3.24/0.86/0.98
I6 (321*481)	27.9/0.44/0.91	19.8/0.77/0.98	2.83/0.81/0.98

the curve. The simpler method is to use the neighborhood average filtering method (Jin & Weng, 2019b; Dong et al., 2019; Liu & Wang, 2020; Gregori, Morillas, Roig, & Sapena, 2018) for φ . The specific analysis of this method can be referred to our published papers. The definition of neighborhood average filtering is as follows:

$$\varphi_L(x) = \text{mean}(\varphi_R(y) | y \in \Omega_x) \quad (27)$$

Where $\varphi(x)$ is the strength of the level set point on x . Ω_x represents a small region with size $(2k + 1) \times (2k + 1)$. mean represents the average intensity value in the calculation window.

The main steps of the algorithm in this paper are shown as:

Input: Input image I .

4 Initialization:

1. linearly stretch I into the range $[0, 1]$;

2. Take logarithm;

3. Set maximum number of iterations N , parameters α , σ and k .

5 Repeat:

Initial the level set function φ as:

$$\varphi(x, t=0) = \begin{cases} -c_0 & x \in \Omega_0 - \partial\Omega_0 \\ 0 & x \in \partial\Omega_0 \\ c_0 & x \in \Omega - \Omega_0 \end{cases} \quad (28)$$

Where $c_0 = 1$. Ω_0 represents the subset of image domain. $\partial\Omega_0$ is the boundary of Ω_0 .

2. Compute β with Eq. (25).

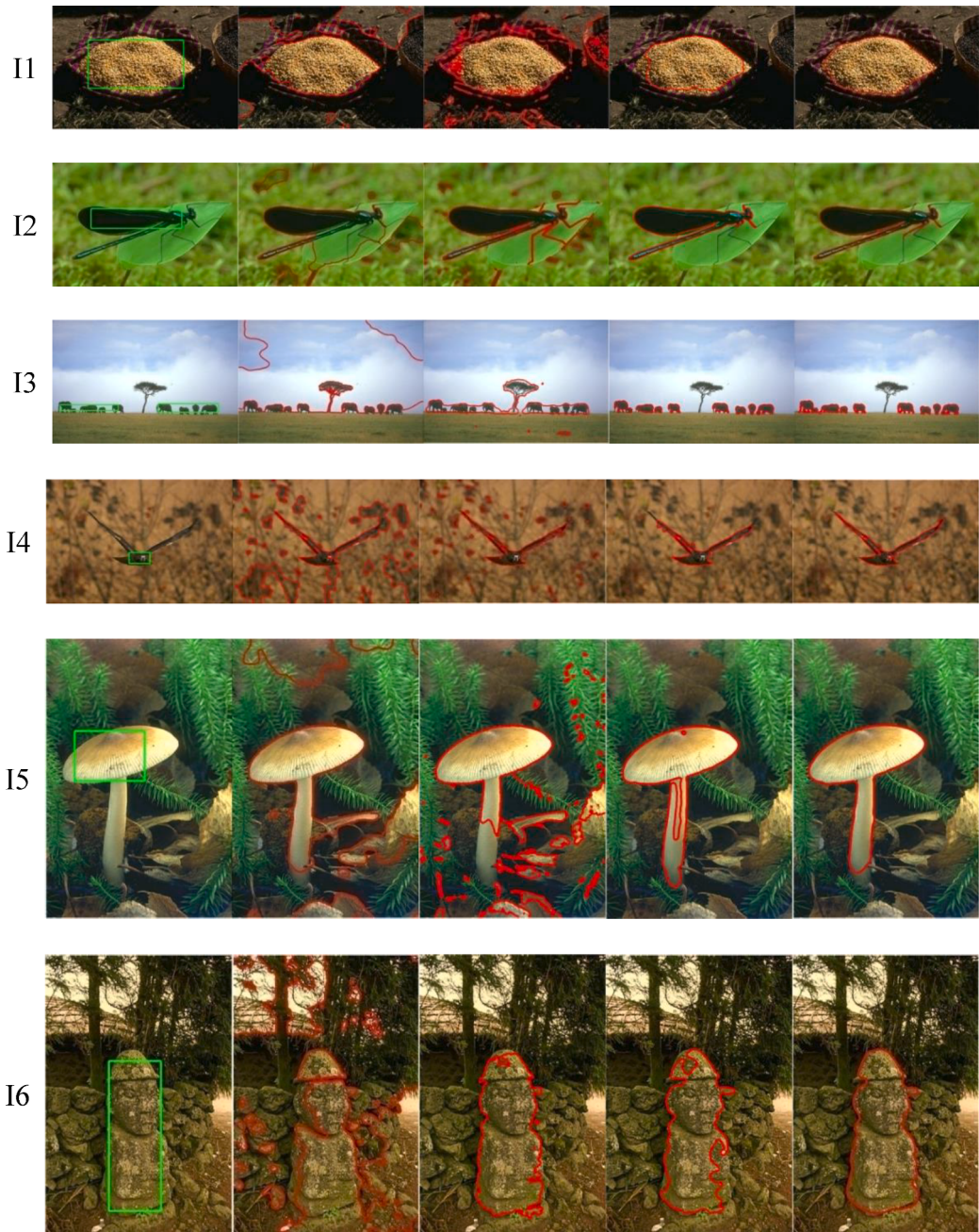


Fig. 8. Comparison experiment with three bias correction ACMs. From left to right: original images and initial contours, segmentation results by the BCACM, LBACM, PBCFCM and ABC models, respectively.

Table3

The CPU runtime, the IOU and the IOU1 of the images in Fig. 7. (Runtime(s)/IOU/IOU1).

	BCACM	LBACM	PBCFCM	ABC
I1 (481*321)	5.14/0.49/ 0.74	62.6/0.73/ 0.91	4.21/0.85/ 0.96	5.72/0.92/ 0.98
I2 (481*321)	10.2/0.44/ 0.83	75.2/0.81/ 0.97	11.9/0.87/ 0.98	12.2/0.88/ 0.98
I3 (481*321)	5.75/0.08/ 0.62	33.5/0.44/ 0.96	4.23/0.83/ 0.99	3.92/0.84/ 0.99
I4 (481*321)	9.31/0.17/ 0.81	45.6/0.56/ 0.97	11.1/0.77/ 0.99	6.10/0.78/ 0.99
I5 (321*481)	8.12/0.42/ 0.82	103/0.53/ 0.90	10.3/0.91/ 0.99	6.61/0.93/ 0.99
I6 (321*481)	5.93/0.36/ 0.66	57.6/0.80/ 0.95	6.5/0.70/ 0.93	3.85/0.81/ 0.95

3. Compute the value of $G_\sigma * 1$ and set an empty reflection image \hat{r} .
 4. Set i from 1 to N .
 5. Compute \hat{b}_1 and \hat{b}_2 with Eq. (19);
 6. Compute with Eq. (20);
 7. Compute gradient descent function with Eq. (24);
 8. Compute level set function evolution $\varphi^{i+1} = \varphi^i + \Delta t \frac{\partial \varphi}{\partial t}$;
 9. Until $\varphi^{i+1} = \varphi^i$, break iteration.
 10. Regularize the level set function φ^{i+1} with Eq. (26);
 11. Compute average neighborhood filtering for φ_R with Eq. (27);
- Output:** level set function $\varphi = \varphi_L$ and segmentation results.
- The main steps of the algorithm in this paper are shown as: <http://github.com/sdjswgr>.

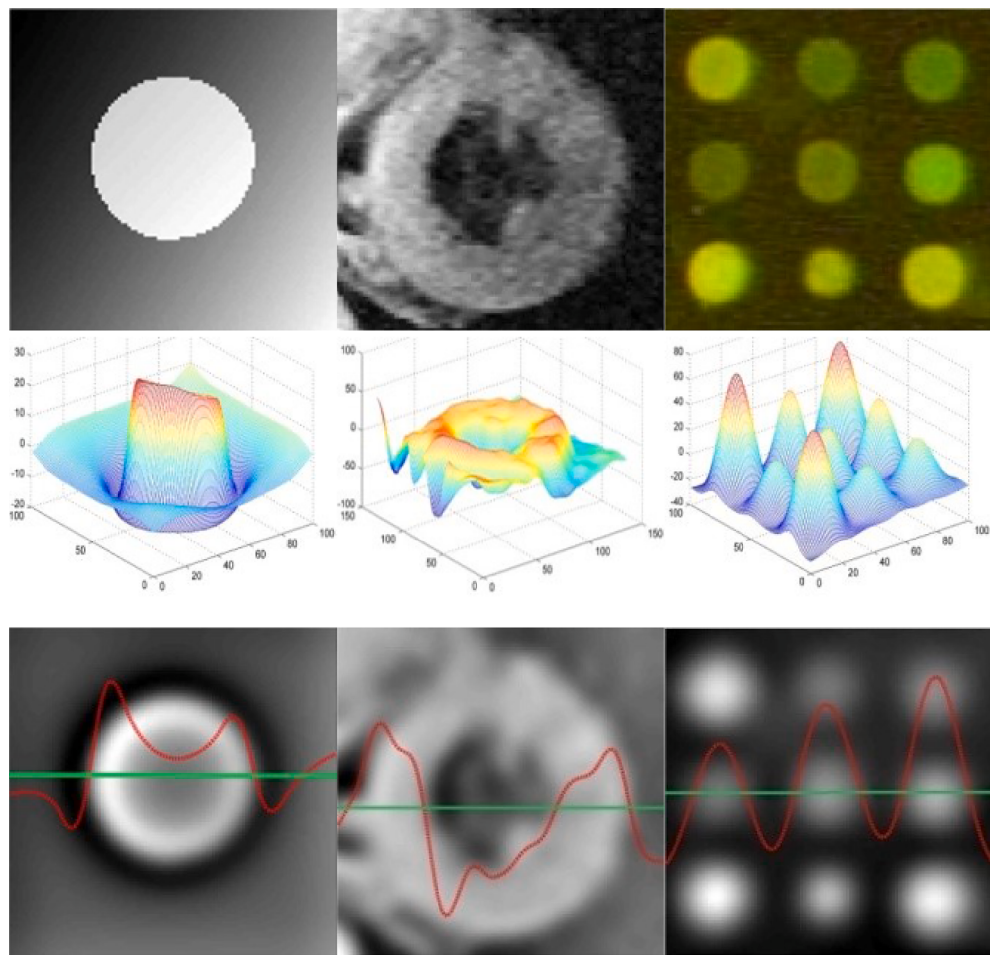


Fig. 9. The reflection image experiment of boundary structure characteristic analysis. From top to bottom: original image, 3-D plots of reflected images and reflection image obtained in the experiment, respectively. In the third row, the green line represents positive values above and negative values below. (For interpretation of the references to colour in this figure legend, the reader is referred to the web version of this article.)

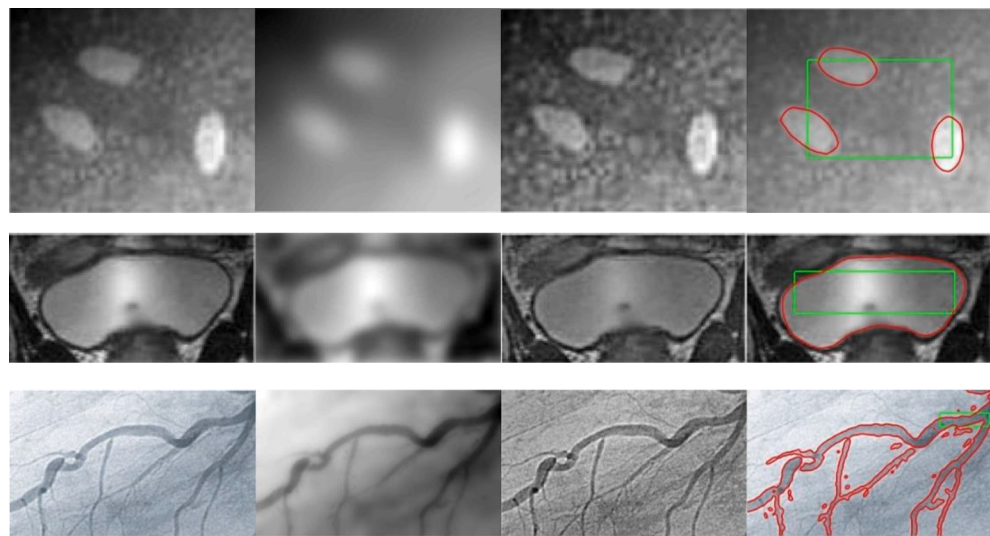


Fig. 10. Results of bias field correction Experiment. From left to right: original image, image of bias field B , bias field correction image and segmentation results, respectively.

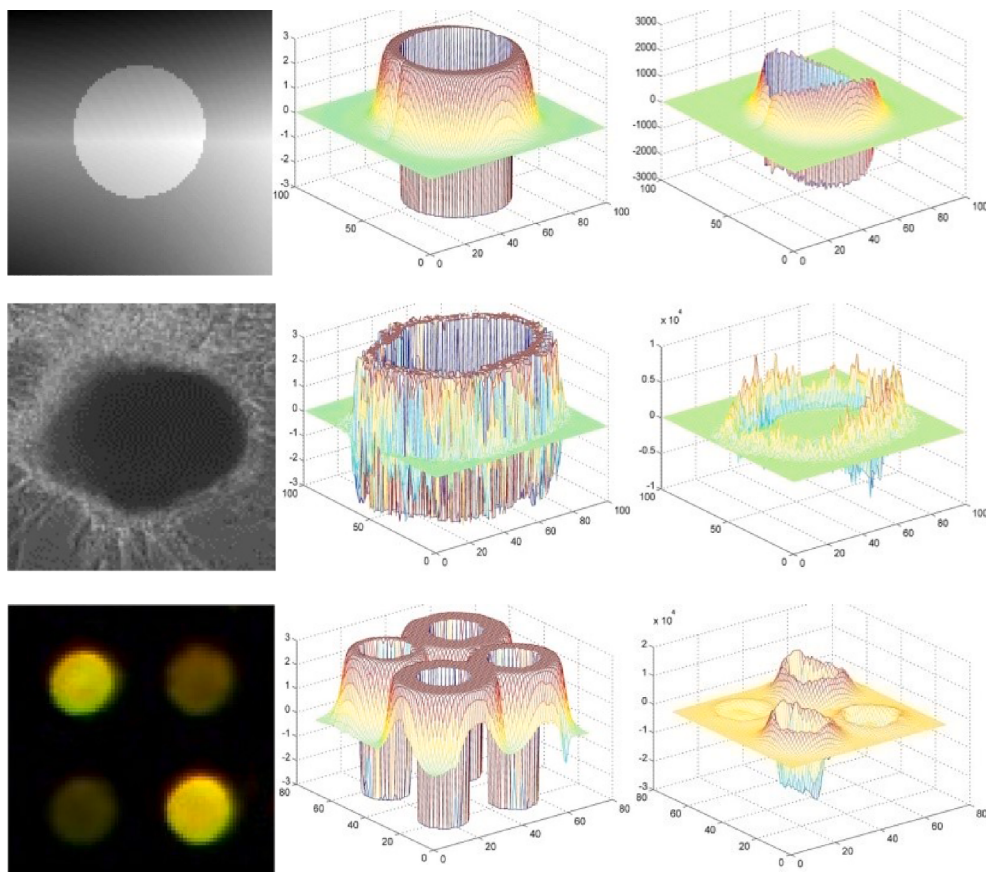


Fig. 11. Comparison experiment of two data-driven terms. From left to right: original images, the proposed adaptive data-driven term and original derived data driver energy, respectively.

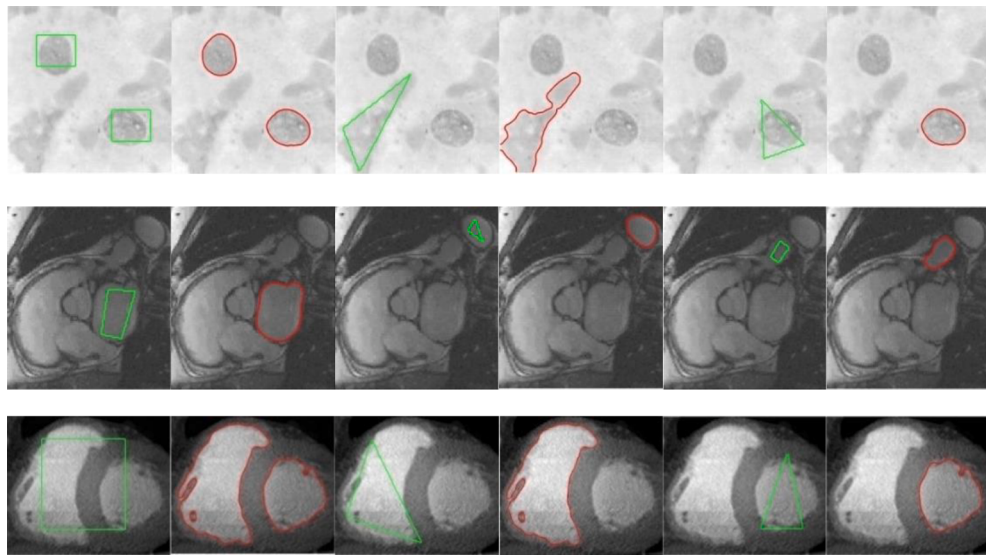


Fig. 12. Segmentation results by the ABC model for three images with different targets.

4. Experiments

4.1. Experiment of additive bias correction theory

First, we use two real images of blood vessels to show the iterative process and segmentation results by the proposed additive bias correction theory. The experiment results are shown in Fig. 2. The green line is

the initial contour line and the red line is the segmentation result. The fifth column of the images in Fig. 2 show the entire iteration process (shown every 5 iterations). Experiment results also show that during the iteration process, the zero level set keeps smooth and the segmentation results are accurate. Secondly, we use four kinds of medical images with different image principles (including Ultrasound image, X-ray image, MR image and Fluorescence image) to verify the segmentation effect of

the additive bias field correction theory. As shown in Fig. 3, we can observe that our model segments this group of images correctly. In a way, our model has good practicality. In Fig. 3, the biased field image is computed as: $b = b_1H + b_2(1 - H)$. Since the ultrasound imaging is characterized by weak target boundaries, the energy of the data-driven term should be reduced in the experiment. The value of parameter α is generally in the range of 1 to 2 in order to prevent the boundary from being broken down. The x-ray image is characterized by strong and uneven reflection background. For such images, the scale parameters of the Gaussian function should be increased and the adjustment range is: $\sigma = 5 \sim 7$. In Fig. 3, parameter α of the first ultrasound image is set to 1.5. Parameter σ of the second X-ray image is set to 7. Other images use default parameters.

4.2. Experiment of robustness to initial contours

Most active contour models are sensitive to the initial contours. Fig. 4 shows the initial contour setting experiment by the proposed model. The results show that our model has better robustness to the initial contour line.

4.3. Experiment of robustness to noise

In order to better verify the proposed additive bias field correction model, we segment the following groups of images, including the images with large individual interference (image a in Fig. 5), the images with strong noise and weak targets (image b in Fig. 5) and the images with uneven illumination (image c and image d in Fig. 5). Experiment results show that the additive bias correction model is robust to uneven illumination and noise interference. In image b and image c, the parameter α is set to 2. Since the target boundary in image b is weak and image c contains strong noise and illumination, we should appropriately reduce the energy of data-driven terms. Meanwhile, for the strong light interference in image d, we can also increase the value of parameter k .

4.4. Comparison with local region-based ACMs

The ABC model is compared with two classic local-region active contour models (RSF (Li et al., 2008), LIF (Zhang et al., 2010)) in this section. The parameter settings of these two models refer to their respective literature. The accuracy used to compare the segmentation results chooses the intersection over union (IOU), which is defined as: $IOU = A_s \cap B_s / A_s \cup B_s$. Where A_s represents the segmented area and B_s represents the real area. The segmented target IOU and background IOU1 are solved respectively. In order to illustrate the speed and accuracy of the model in this paper, two standard image libraries are introduced. Fig. 6 shows the segmentation results of five images in the standard image libraries.

4.5. Comparison with state-of-the-art ACMs

The LPF&FCM model (Ding, Xiao, & Weng, 2018) is a pre-fitting hybrid active contour model. This model uses the local fuzzy c-means clustering (FCM) method (Memon & Lee, 2018; Yang & Nataliani, 2017) to compute the fitting function in advance, which reduces the running time of the iteration. At the same time, the segmentation precision of this model is relatively high. The idea of the RSF&LoG (Ding et al., 2017) model is to add a second-order differential operator edge detection operator and combine with the data-driven items in the RSF model. The purpose of the above operation is to increase the edge effect in the data-driven items and improve the segmentation accuracy. Fig. 7 compares the RSF&LoG model, LPF&FCM model and the proposed model based on speed and accuracy. Six images with complex targets are selected in this section. Fig. 7 and Table 2 show that the ABC model has obvious advantages, especially in terms of speed.

4.6. Comparison with bias correction ACMs

Recently, there are three typical models in the research of multiplicative bias correction, including the BCACM (Li et al., 2011) model, the LBACM (Zhang et al., 2016) model and the PBCFCM (Jin & Weng, 2019b) model. The results in Fig. 8 and Table 3 show that the BCACM model and the LBACM model are sensitive to local intensity inhomogeneity and slow in operation. Of course, part of the reason is related to the natural image selected in this experiment. Natural images have the characteristics of complex background and strong interference. The PBCFCM model uses a pre-biased field correction method to overcome the problem of local intensity inhomogeneity. This process can greatly improve the segmentation effect, but also increases segmenting time. Experiment results show that the ABC model is much more accurate and faster than these three typical multiplicative bias field models.

5. Discussion

5.1. Feature analysis of reflected images

The image model in Eq. (12) indicates that the reflected image effectively reflects the uneven boundary structure and weakens the uneven illumination. Fig. 9 shows the experiment results of the reflected images. From the experiment results we can observe that the reflected image represents the second-order differential characteristic (Somasundaram & Shanmugavadi, 2008) of the image. However, it is different from the standard second-order differential. In fact the reflection image shows the structural features of the boundary, while the boundary point of the image is reflected at the zero crossing of the curve. The curve of the reflected image rises rapidly from a negative value to a positive value area, which means that the image region enters the bright area from the dark area. Otherwise, it means that the image point enters the dark area. The traditional multiplication model cannot effectively solve the phenomenon of uneven illumination, while the additive bias correction model has ideal effect.

5.2. Experiment on the effect of additive bias correction

Additive bias correction theory can effectively correct illumination interference. We perform experiments on three medical images with uneven illumination interference in this section. After additive bias correction, image is converted to: $i_b = i - b$. Where bias field $b = b_1H + b_2(1 - H)$. Experiment results are shown in Fig. 10. The diagram of bias field correction proves that the illumination inequality of the original image is greatly improved after additive bias correction. The third column shows the bias field correction image with reduced illumination interference and enhanced boundary features.

5.3. Robustness of data-driven energy

Due to the diversity of image types, the brightness and contrast of each image are quite different. When the energy parameter in Eq. (23) is debugged, we find that the parameters of most images are different and vary greatly. The robustness experiment of data-driven energy is shown in Fig. 11. The third column in Fig. 11 reflects the original derived data-driven energy. The third image in Fig. 11 is characterized by multiple targets and the size of each target is different. This phenomenon brings great uncertainty to the traditional active contour model. The adaptive data-driven term in Eq. (24) solves the problem of energy unification, which greatly improves the robustness of the proposed model. In addition, the data-driven term is controlled within a certain range and the iterative energy is effectively controlled, which has advantages in the segmentation of medical images with complex backgrounds. As shown in Fig. 12, by reducing the value of coefficient α appropriately, the proposed model can freely select each target object without affecting other surrounding targets.

5.4. Discussion with parameter setting

Due to the problems of target size, intensity, noise and image contrast, the parameters of the proposed model should be adjusted according to different types of images.

- A) For images with large targets and clear boundaries (such as Fig. 6-I3, Fig. 7-I3, I4 and I5, Fig. 8-I5), the window size k should be increased to include large target, otherwise it will be reduced.
- B) If the intensity of the target is weak (such as the first row of Fig. 4), the value of α should be increased. Increasing α is conducive to speed up the iteration. However, if the target boundary is fuzzy, the value of α should be reduced to prevent the target boundary from being broken down.
- C) For images with uneven lighting or serious background interference, the value of Gaussian scaling parameter σ should be increased moderately (such as Fig. 3-image a, Fig. 6-I2, Fig. 7-I3 and Fig. 8-I1).

From the perspective of imaging principle, the characteristic of ultrasonic image is that the target boundary is generally weak. The corresponding value of α is generally set as 1 ~ 2 to prevent the boundary from breaking down. X-ray image is characterized by strong and uneven reflection background of the target. Therefore, the scaling parameter of σ should be increased as 5–7.

5.5. Application of the regularization method

The proposed model is mainly applied to two-phase images. Our model cannot handle objects with distinct multiple colors (Martin, Fowlkes, Tal, & Malik, 2001; Yin, Qian, & Gong, 2017). For example, a target object contains both black and white targets, or a target object contains shadows that are obscured by light. The main reason is that the intensity values of image objects are obviously different or opposite. The proposed model can only obtain the deeper or whiter regions for the segmentation of the above images, and cannot obtain the correct segmentation results. In the future, we will consider using the multi-phase segmentation (Yang & Nataliani, 2017; Nguyen, Dahl, & Bærentzen, 2019) to solve this problem.

6. Conclusions

This paper presents an additive bias correction model based on strength inhomogeneity. The proposed model divides the image into three parts: additive bias field function, structure function of reflection edge and Gaussian noise. Each component of the additive image model has a clear physical concept. Compared with the traditional multiplicative model, the addition model has faster calculation speed. The proposed model can obtain ideal segmentation effect for images with intensity inhomogeneity. The level set function is introduced to transform the local clustering criterion into the energy function. An optimized adaptive data driven term is designed to solve the problem of energy unification and improve the robustness. For pictures with different sizes and features, there is no need to adjust the parameters repeatedly. A novel de-parameterized regularization function is proposed to improve the slope of the function through the zero point and smooths other regions, thus improving the robustness of the model. Experiments show the segmentation performance of the proposed model. Compared with other classical active contour models, the proposed model has faster segmentation speed, higher accuracy and better robustness. One shortcoming of the proposed model is that it is not suitable for segmenting objects with obvious multiple colors since the intensity values of image objects are different. The proposed model can only obtain the deeper or whiter regions for the segmentation of the above images.

In the future work, we will consider the multi-phase segmentation,

which uses multiple level set functions on the basis of the proposed model and attach corresponding constraints. Considering the outstanding performance of deep-learning based method (Zhang et al., 2010; Karimi et al., 2019) in image segmentation, we may study and apply Self-Organizing Maps to our future research.

CRediT authorship contribution statement

Guirong Weng: Methodology, Software, Validation, Formal analysis, Investigation, Writing – original draft. **Bin Dong:** Conceptualization, Supervision, Project administration, Funding acquisition, Writing - review & editing. **Yu Lei:** Resources, Data curation, Visualization.

Declaration of Competing Interest

The authors declare that they have no known competing financial interests or personal relationships that could have appeared to influence the work reported in this paper.

Acknowledgement

This work is supported by the National Nature Science Foundation of China [grant No. 61873176].

References

- Banan, A., Nasiri, A., & Taheri-Garavand, A. (2020). Deep learning-based appearance features extraction for automated carp species identification. *Aquacultural Engineering*, 89(December 2019), 102053. <https://doi.org/10.1016/j.aquaeng.2020.102053>.
- Cai, Q., Liu, H., Zhou, S., Sun, J., & Li, J. (2018). An adaptive-scale active contour model for inhomogeneous image segmentation and bias field estimation. *Pattern Recognition*, 82, 79–93. <https://doi.org/10.1016/j.patcog.2018.05.008>
- Caselles, V., Catté, F., Coll, T., & Dibos, F. (1993). A geometric model for active contours in image processing. *Numerische Mathematik*, 66(1), 1–31. <https://doi.org/10.1007/BF01385685>
- Chan, S., Yang, X., Chen, G., Pu, J., Shi, D., Wang, L., & Chang, Y. (2018). Active contours driven by edge entropy fitting energy for image segmentation. *Signal Processing*, 149, 27–35. <https://doi.org/10.1016/j.sigpro.2018.02.025>
- Chan, T. F., & Vese, L. A. (1977). Active contours without edges. *British Dental Journal*, 10 (2), 266–277. <https://doi.org/10.1109/83.902291>
- Ding, K., Xiao, L., & Weng, G. (2017). Active contours driven by region-scalable fitting and optimized Laplacian of Gaussian energy for image segmentation. *Signal Processing*, 134(50), 224–233. <https://doi.org/10.1016/j.sigpro.2016.12.021>
- Ding, K., Xiao, L., & Weng, G. (2018). Active contours driven by local pre-fitting energy for fast image segmentation. *Pattern Recognition Letters*, 104, 29–36. <https://doi.org/10.1016/j.patrec.2018.01.019>
- Dong, B., Jin, R., & Weng, G. (2019). Active contour model based on local bias field estimation for image segmentation. *Signal Processing: Image Communication*, 78(178), 187–199. <https://doi.org/10.1016/j.image.2019.07.001>
- Fan, Y., Xu, K., Wu, H., Zheng, Y., & Tao, B. O. (2020). Spatiotemporal modeling for nonlinear distributed thermal processes based on KL decomposition, MLP and LSTM Network. *IEEE Access*, 8, 25111–25121. <https://doi.org/10.1109/ACCESS.2020.2970836>
- Gregori, V., Morillas, S., Roig, B., & Sapena, A. (2018). Fuzzy averaging filter for impulse noise reduction in colour images with a correction step. *Journal of Visual Communication and Image Representation*, 55(July), 518–528. <https://doi.org/10.1016/j.jvcir.2018.06.025>
- Huang, Z. K., & Chau, K. W. (2008). A new image thresholding method based on Gaussian mixture model. *Applied Mathematics and Computation*, 205(2), 899–907. <https://doi.org/10.1016/j.amc.2008.05.130>
- Horn, B. K. P. (1974). Determining lightness from an image. *Computer Graphics and Image Processing*, 3(4), 277–299.
- Jia, W., Ling, B., Chau, K. W., & Heutte, L. (2008). Palmprint identification using restricted fusion. *Applied Mathematics and Computation*, 205(2), 927–934. <https://doi.org/10.1016/j.amc.2008.05.024>
- Jin, R., & Weng, G. (2019a). A robust active contour model driven by fuzzy c-means energy for fast image segmentation. *Digital Signal Processing: A Review Journal*, 90, 100–109. <https://doi.org/10.1016/j.dsp.2019.04.004>
- Jin, R., & Weng, G. (2019b). A robust active contour model driven by pre-fitting bias correction and optimized fuzzy c-means algorithm for fast image segmentation. *Neurocomputing*, 359(xxxx), 408–419. <https://doi.org/10.1016/j.neucom.2019.06.019>
- Jin, R., & Weng, G. (2019c). Active contour model based on improved fuzzy c-means algorithm and adaptive functions. *Computers and Mathematics with Applications*, 78 (11), 3678–3691. <https://doi.org/10.1016/j.camwa.2019.06.010>

- Jin, R., & Weng, G. (2019d). Active contours driven by adaptive functions and fuzzy c-means energy for fast image segmentation. *Signal Processing*, 163, 1–10. <https://doi.org/10.1016/j.sigpro.2019.05.002>
- Karimi, D., Zeng, Q.i., Mathur, P., Avinash, A., Mahdavi, S., Spadinger, I., ... Salcudean, S. E. (2019). Accurate and robust deep learning-based segmentation of the prostate clinical target volume in ultrasound images. *Medical Image Analysis*, 57, 186–196. <https://doi.org/10.1016/j.media.2019.07.005>
- Li, C., Gore, J. C., & Davatzikos, C. (2014). Multiplicative intrinsic component optimization (MICO) for MRI bias field estimation and tissue segmentation. *Magnetic Resonance Imaging*, 32(7), 913–923. <https://doi.org/10.1016/j.mri.2014.03.010>
- Li, C., Huang, R., Ding, Z., Gatenby, J. C., Metaxas, D. N., & Gore, J. C. (2011). A level set method for image segmentation in the presence of intensity inhomogeneities with application to MRI. *IEEE Transactions on Image Processing*, 20(7), 2007–2016. <https://doi.org/10.1109/TIP.2011.2146190>
- Li, C., Kao, C. Y., Gore, J. C., & Ding, Z. (2007). Implicit active contours driven by local binary fitting energy. In *Proceedings of the IEEE Computer Society Conference on Computer Vision and Pattern Recognition*. <https://doi.org/10.1109/CVPR.2007.383014>
- Li, C., Kao, C. Y., Gore, J. C., & Ding, Z. (2008). Minimization of region-scalable fitting energy for image segmentation. *IEEE Transactions on Image Processing*, 17(10), 1940–1949. <https://doi.org/10.1109/TIP.2008.2002304>
- Li, C., Xu, C., Gui, C., & Fox, M. D. (n.d.). Level Set EvolutionWithout Re-initialization: A New Variational Formulation.
- Li, C., Xu, C., Gui, C., & Fox, M. D. (2010). Distance regularized level set evolution and its application to image segmentation. *IEEE Transactions on Image Processing*, 19(12), 3243–3254. <https://doi.org/10.1109/TIP.2010.2069690>
- Liu, W., & Wang, Z. (2020). A novel multi-focus image fusion method using multiscale shearing non-local guided averaging filter. *Signal Processing*, 166, 107252. <https://doi.org/10.1016/j.sigpro.2019.107252>
- Martin, D., Fowlkes, C., Tal, D., & Malik, J. (2001). A database of human segmented natural images and its application to evaluating segmentation algorithms and measuring ecological statistics. *Proceedings of the IEEE International Conference on Computer Vision*, 2, 416–423. <https://doi.org/10.1109/ICCV.2001.937655>
- Md. Golam Moazzam, M. G. M. (2013). Medical Image Segmentation Based on Level Set Method. *IOSR Journal of Computer Engineering*, 10(6), 35–41. <https://doi.org/10.9790/0661-1063541>
- Memon, K. H., & Lee, D. H. (2018). Generalised kernel weighted fuzzy C-means clustering algorithm with local information. *Fuzzy Sets and Systems*, 340, 91–108. <https://doi.org/10.1016/j.fss.2018.01.019>
- Nguyen, T. T., Dahl, V. A., & Berentzen, J. A. (2019). Multi-phase image segmentation with the adaptive deformable mesh. *Pattern Recognition Letters*, 117, 97–103. <https://doi.org/10.1016/j.patrec.2018.12.009>
- Somasundaram, K., & Shanmugavadivu, P. (2008). Impulsive noise detection by second-order differential image and noise removal using adaptive nearest neighbourhood filter. *AEU - International Journal of Electronics and Communications*, 62(6), 472–477. <https://doi.org/10.1016/j.aeue.2007.07.001>
- Vicent, C., Ron, K., & Guillermo, S. (1997). Geodesic active contours. *International Journal of Computer Vision*, 22(1), 61–79. <https://doi.org/10.1023/A:1007979827043>
- Yang, M., & Nataliani, Y. (2017). Robust-learning fuzzy c-means clustering algorithm with unknown number of clusters. *Pattern Recognition*, 71, 45–59. <https://doi.org/10.1016/j.patcog.2017.05.017>
- Yin, S., Qian, Y., & Gong, M. (2017). Unsupervised hierarchical image segmentation through fuzzy entropy maximization. *Pattern Recognition*, 68, 245–259. <https://doi.org/10.1016/j.patcog.2017.03.012>
- Zhang, K., Song, H., & Zhang, L. (2010). Active contours driven by local image fitting energy. *Pattern Recognition*, 43(4), 1199–1206. <https://doi.org/10.1016/j.patcog.2009.10.010>
- Zhang, K., Zhang, L., Lam, K.-M., & Zhang, D. (2016). A level set approach to image segmentation with intensity inhomogeneity. *IEEE Transactions on Cybernetics*, 46(2), 546–557. <https://doi.org/10.1109/TCYB.622103610.1109/TCYB.2015.2409119>
- Zhou, S., Wang, J., Zhang, M., Cai, Q., & Gong, Y. (2017). Correntropy-based level set method for medical image segmentation and bias correction. *Neurocomputing*, 234 (August 2016), 216–229. <https://doi.org/10.1016/j.neucom.2017.01.013>.